



THE UNIVERSITY *of* EDINBURGH

## Edinburgh Research Explorer

### Conservation of the structural and functional architecture of encapsulated ferritins in bacteria and archaea

**Citation for published version:**

He, D, Piergentili, C, Ross, J, Tarrant, E, Tuck, LR, Mackay, CL, Mciver, Z, Waldron, KJ, Clarke, DJ & Marles-wright, J 2019, 'Conservation of the structural and functional architecture of encapsulated ferritins in bacteria and archaea', *Biochemical Journal*, vol. 476, no. 6, pp. 975-989.  
<https://doi.org/10.1042/BCJ20180922>

**Digital Object Identifier (DOI):**

[10.1042/BCJ20180922](https://doi.org/10.1042/BCJ20180922)

**Link:**

[Link to publication record in Edinburgh Research Explorer](#)

**Document Version:**

Peer reviewed version

**Published In:**

Biochemical Journal

**General rights**

Copyright for the publications made accessible via the Edinburgh Research Explorer is retained by the author(s) and / or other copyright owners and it is a condition of accessing these publications that users recognise and abide by the legal requirements associated with these rights.

**Take down policy**

The University of Edinburgh has made every reasonable effort to ensure that Edinburgh Research Explorer content complies with UK legislation. If you believe that the public display of this file breaches copyright please contact [openaccess@ed.ac.uk](mailto:openaccess@ed.ac.uk) providing details, and we will remove access to the work immediately and investigate your claim.



1 **Conservation of the structural and functional architecture of encapsulated ferritins in**  
2 **bacteria and archaea**

3

4 Didi He<sup>1,#,\*</sup>, Cecilia Piergentili<sup>2,\*</sup>, Jennifer Ross<sup>3,\*</sup>, Emma Tarrant<sup>4</sup>, Laura R. Tuck<sup>1</sup>, C. Logan  
5 Mackay<sup>3</sup>, Zak Mclver<sup>2</sup>, Kevin J. Waldron<sup>4</sup>, David J. Clarke<sup>3\*</sup>, Jon Marles-Wright<sup>2\*</sup>,

6 <sup>1</sup>Institute of Quantitative Biology, Biochemistry and Biotechnology, School of Biological Sciences,  
7 The University of Edinburgh, Max Born Crescent, Edinburgh, EH9 3BF; <sup>2</sup>School of Natural and  
8 Environmental Sciences, Newcastle University. Newcastle upon Tyne, NE1 7RU; <sup>3</sup>EaStCHEM  
9 School of Chemistry, The University of Edinburgh, Joseph Black Building, David Brewster Road,  
10 Edinburgh, Scotland, EH9 3FJ; <sup>4</sup>Institute for Cell and Molecular Biosciences, Newcastle University,  
11 Newcastle upon Tyne, NE2 4HH.

12 *#Current address: Structural Genomics Consortium, University of Oxford, Old Road Campus*  
13 *Research Building, Roosevelt Drive, Oxford, OX3 7DQ*

14

15 Running title: Structure and function of EncFtn homologues

16

17 \* These authors contributed equally to this work

18 \* To whom correspondence should be addressed:

19 Jon Marles-Wright, +44(0)191 208 4855, [Jon.marles-wright1@ncl.ac.uk](mailto:Jon.marles-wright1@ncl.ac.uk);

20 David J. Clarke, +44(0)131 650 4808, [Dave.clarke@ed.ac.uk](mailto:Dave.clarke@ed.ac.uk).

21

22 *KEYWORDS: encapsulin, encapsulated ferritin, ferritin, ferroxidase, mass spectrometry (MS),*  
23 *metalloprotein, protein assembly, Pyrococcus furiosus, Haliangium ochraceum, X-ray*  
24 *crystallography*

25

26 **Abstract**

27 Ferritins are a large family of intracellular proteins that protect the cell from oxidative stress by  
28 catalytically converting Fe(II) into less toxic Fe(III) and storing iron minerals within their core.  
29 Encapsulated ferritins (EncFtn) are a sub-family of ferritin-like proteins, which are widely distributed  
30 in all bacterial and archaeal phyla. The recently characterized *Rhodospirillum rubrum* EncFtn  
31 displays an unusual structure when compared to classical ferritins, with an open decameric structure  
32 that is enzymatically active, but unable to store iron. This EncFtn must be associated with an  
33 encapsulin nanocage in order to act as an iron store. Given the wide distribution of the EncFtn family  
34 in organisms with diverse environmental niches, a question arises as to whether this unusual  
35 structure is conserved across the family. Here, we characterize EncFtn proteins from the  
36 halophile *Haliangium ochraceum* and the thermophile *Pyrococcus furiosus*, which show the  
37 conserved annular pentamer of dimers topology. Key structural differences are apparent between  
38 the homologues, particularly in the centre of the ring and the secondary metal binding site, which is  
39 not conserved across the homologues. Solution and native mass spectrometry analyses highlight  
40 that the stability of the protein quaternary structure differs between EncFtn proteins from different  
41 species. The ferroxidase activity of EncFtn proteins was confirmed, and we show that while the  
42 quaternary structure around the ferroxidase centre is distinct to classical ferritins, the ferroxidase  
43 activity is still inhibited by Zn(II). Our results highlight the common structural organization and activity  
44 of EncFtn proteins, despite diverse host environments and contexts within encapsulins.

45

## 46 **Introduction**

47 The encapsulated ferritins (**EncFtn**) are recently described members of the ferritin superfamily [1–  
48 3]. These proteins are sequestered within encapsulin nanocompartments, and the two proteins act  
49 in concert to provide an iron storage system with a much greater capacity than the classical ferritins  
50 and DNA-binding Protein from Starved cells (DPS) nanocages [3,4]. Genes encoding encapsulin-  
51 associated ferritins have been identified in a wide range of bacterial and archaeal species that inhabit  
52 diverse ecological niches from ponds, streams (*Rhodospirillum rubrum*), and coastal seas  
53 (*Haliangium ochraceum*), to abyssal ocean vents (*Pyrococcus furiosus*) [5].

54 The *R. rubrum* EncFtn was the first protein in its family to be structurally and biochemically  
55 characterized; it has a fold with two antiparallel alpha-helices that adopts an annular-decamer  
56 quaternary structure, assembled as a pentamer of dimers [1]. The subunits dimerize through metal-  
57 mediated contacts to reconstitute the four-helix ferritin fold with a functional ferroxidase centre [6,7].  
58 While the EncFtn protein displays ferroxidase activity, it is not capable of storing iron in the same  
59 way as other ferritins due to its open architecture and the lack of an enclosed cavity for iron  
60 mineralization [8,9]; therefore, EncFtn family proteins must be localized to the interior of an  
61 encapsulin nanocage for efficient iron storage [1,3,5]. Localization to encapsulin nanocages is  
62 mediated by a short encapsulation sequence, which is usually appended to the C-terminus of the  
63 EncFtn protein chain [1,3,5,10]; addition of this sequence to heterologous proteins is sufficient to  
64 direct them to the lumen of encapsulins [11,12].

65 The encapsulin protein family is structurally related to the HK97 bacteriophage shell protein and they  
66 form icosahedral nanocages of between 25 and 35 nm in diameter. Pores are formed at the  
67 icosahedral symmetry axes between subunits to allow substrate access to encapsulated enzyme  
68 cargoes [3,5,10,13]. The *R. rubrum* encapsulin was shown to associate with over 2000 iron ions per  
69 capsid, while being catalytically inactive; and, in concert with EncFtn, capable of mineralizing and  
70 storing more than four times as much iron as a classical ferritin nanocage [1]. Given the wide  
71 distribution of encapsulin proteins across bacterial and archaeal phyla, and the conservation of the  
72 EncFtn proteins in 20 % of all phyla with encapsulin genes, we investigated the structure and activity  
73 of EncFtn proteins from the halophilic Proteobacterium *H. ochraceum* and the EncFtn-fusion from

74 the Euryarchaeota *P. furiosus*, to determine whether the structural and functional organization seen  
75 in the *R. rubrum* EncFtn is conserved within its phylum and between domains and environmental  
76 niches.

77 Here we report the structural and biochemical characterization of members of the EncFtn family from  
78 *H. ochraceum* and *P. furiosus*. Both proteins adopt similar topology to the *R. rubrum* EncFtn and  
79 assemble as annular decamers formed from pentamers of dimers, with ferroxidase centres located  
80 at one of the dimer interfaces. The ferroxidase activities of the proteins are comparable, and they  
81 show similar levels of inhibition by the competing metal ion zinc. These data show that the structural  
82 and biochemical features of encapsulated ferritins are conserved across different environmental  
83 niches and phyla with particular adaptations for thermal stability in thermophilic microorganisms.

84

## 85 **Materials and Methods**

### 86 *Cloning expression and purification of EncFtn and EncFtn homologues*

87 Recombinant encapsulated ferritin from *Rhodospirillum rubrum* was produced as described  
88 previously [1]. DNA fragments encoding truncated versions of the encapsulated ferritins from  
89 *Haliangium ochraceum* (Hoch\_3836<sub>1-98</sub>) (Uniprot: D0LZ73\_HALO1) and *Pyrococcus furiosus*  
90 (Pfc\_01575<sub>1-99</sub>) (Uniprot: I6U7J4\_9EURY) were produced as double-stranded gBlocks (IDT) and  
91 codon optimized for expression in *E. coli*, with restriction endonuclease sites for insertion into pET-  
92 28a (Pfc\_05157<sub>1-99</sub>) or a modified pET-28 vector with CIDAR MoClo [14] Golden Gate cloning sites  
93 (Hoch\_3836<sub>1-98</sub>). Untagged and His-tagged variants were produced for both proteins in this way. A  
94 StrepII-tagged variant of each protein was produced by assembly of the EncFtn gBlock into a CIDAR  
95 MoClo destination vector with a custom T7 promoter and StrepII-tag terminator part. Sequences of  
96 primers and gBlocks used in this study are shown in Tables S1 and S2 respectively, and the  
97 sequences of expressed proteins are shown in Table S3. The expression plasmids were transformed  
98 into *E. coli* BL21(DE3) cells and a single colony was grown overnight at 37 °C in 100 ml LB medium,  
99 supplemented with 35 µg/ml kanamycin, with shaking at 180 rpm. The cells were sub-cultured into  
100 1 L of LB or M9 minimal medium, grown until OD<sub>600</sub>=0.6, and protein production was induced with  
101 1 mM IPTG, the temperature was reduced to 18 °C and cells were incubated for a further 18 hours.  
102 Cells were harvested by centrifugation at 4,000 × *g* and washed with PBS. Cell-free extract was  
103 produced by resuspending cells in 10 x v/w Buffer A (50 mM Tris-HCl, pH 8.0) and sonicated on ice  
104 for 5 minutes with 30 s on/off cycle at 60 watts power output. The lysate was cleared by centrifugation  
105 at 35,000 × *g* and filtered with a 0.45 µm syringe filter. Untagged recombinant proteins were purified  
106 from cell-free extract by anion exchange using HiPrep Q sepharose fast-flow 16/10 column (GE  
107 Healthcare) equilibrated with Buffer A. Cell free extract was applied to the column and unbound  
108 proteins were washed off with 10 column volumes of Buffer A. Proteins were eluted with a linear  
109 gradient of Buffer B (50 mM Tris-HCl, pH 8.0, 1 M NaCl) over 20 column volumes and fractions  
110 collected.  
111 His-tagged proteins were purified by resuspending cells in 10 x (v/w) Buffer HisA (50 mM Tris-HCl,  
112 pH 8.0, 500 mM NaCl, 50 mM imidazole) before sonication and clarification as above. Clarified cell

113 lysate was applied to a 5 ml HisTrap FF column (GE Healthcare) and unbound proteins were washed  
114 off with 10 column volumes of Buffer HisA. A step-gradient of 50 % and 100 % Buffer HisB (50 mM  
115 Tris-HCl, pH 8.0, 500 mM NaCl, 500 mM imidazole) was used to elute His-tagged proteins.

116 Fractions of Q sepharose or His-trap eluent containing the protein of interest, as identified by 15 %  
117 (w/v) SDS-PAGE, were subjected to size-exclusion chromatography using an S200 16/60 column,  
118 previously calibrated with LMW/HMW calibration kits (GE Healthcare) (Fig. S1) and equilibrated with  
119 Buffer GF (50 mM Tris-HCl, pH 8.0, 150 mM NaCl).

120 StrepII-tagged proteins were purified by suspending cells in 10 x (v/w) Buffer W (100 mM Tris pH  
121 8.0, 150 mM NaCl) before sonication and clarification as described above. Cell lysate was applied  
122 to Strep-Trap HP column (GE Healthcare), prepared as suggested by the manufacturer, and  
123 unbound proteins were washed off by applying 5 column volumes of Buffer W. Strep-tagged proteins  
124 were eluted by Buffer E (100 mM Tris pH 8.0, 150 mM NaCl, 2.5 mM desthiobiotin). Eluted protein  
125 was buffer-exchanged to Buffer GF by centrifugal concentrator Vivaspin Turbo (Sartorius, 10 kDa  
126 MWCO) to remove desthiobiotin.

### 127 ***Protein quantification***

128 Purified protein concentration was determined by colorimetric technique using the Pierce™ BCA  
129 protein assay kit following manufacturer specifications for the standard Test-tube procedure at 37  
130 °C. Diluted bovine serum albumin (BSA) standards were prepared in GF buffer. Fig. S2A/B show  
131 colour response curves prepared for His-tagged or Strep-tagged protein quantification, respectively.  
132 Protein samples absorbance at 562 nm (average of 3 experimental replicates) are listed in Table  
133 S4.

### 134 ***Ferroxidase assays***

135 Ferroxidase activity of the enzymes was tested by following the formation of Fe(III) species by UV-  
136 visible spectroscopy at 20 °C, as previously described [1]. Oxygen-free aliquots of Fe(II) (1 mM)  
137 were prepared by dissolving FeSO<sub>4</sub>·7H<sub>2</sub>O in 0.1 % (v/v) HCl under anaerobic conditions. Purified  
138 proteins (decameric fraction) were diluted anaerobically to the final concentration of 10 μM monomer  
139 in Buffer H (10 mM HEPES pH 8.0, 150 mM NaCl). Protein and Fe(II) samples were added to a

140 quartz cuvette (Hellma) under aerobic conditions at the final concentration of 10 and 50  $\mu\text{M}$ ,  
141 respectively. Absorbance at 315 nm was monitored every second over 1500 s using a UV-visible  
142 spectrophotometer (Perkin Elmer Lambda 35) using the provided TimeDrive software. A negative  
143 control was performed by monitoring the progress curve at  $A_{315}$  of Fe(II) salt sample in the absence  
144 of protein. Data presented here are the mean of three technical replicates of time zero-subtracted  
145 progress curves with standard deviations calculated from the mean.

#### 146 *Zinc inhibition of ferroxidase activity*

147 In order to test enzyme selectivity toward Fe(II), the ferroxidase assay was carried out as previously  
148 described [1], in the presence of  $\text{FeSO}_4 \cdot 7\text{H}_2\text{O}$  (50  $\mu\text{M}$ ) and various concentrations of  $\text{ZnSO}_4 \cdot 2\text{H}_2\text{O}$ .  
149 The  $A_{315}$  nm progress curve of protein mixed with the highest concentration of Zn(II) used in the  
150 assay (100  $\mu\text{M}$ ) was also monitored as a negative control.

#### 151 *Protein Crystallography*

152 Hoch\_EncFtn and Pfc\_EncFtn were concentrated to 10 mg/ml using a 10 kDa MWCO centrifugal  
153 concentrator (Vivaspin) and subjected to sitting drop vapor diffusion crystallization using 70  $\mu\text{l}$  well  
154 solution and drops of 100 nl protein, plus 100 nl well solution. Crystals of Hoch\_EncFtn grew in well  
155 solution containing 0.2 M NaCl, 0.1 M Bis-Tris, pH 5.5, 20 % (w/v) PEG 3350; and crystals of  
156 Pfc\_EncFtn were found in a condition containing 0.2 M  $\text{LiSO}_4 \cdot \text{H}_2\text{O}$ , 20 % (w/v) PEG 3350. Crystals  
157 were harvested using a LithoLoop (Molecular Dimensions Limited), transferred to a cryoprotection  
158 solution of well solution supplemented with 20 % (v/v) PEG 200 and flash cooled in liquid nitrogen.  
159 Diffraction data were collected at Diamond Light Source at 100 K using a Pilatus 6M detector. Images  
160 were integrated and scaled using XDS [15]; the correct crystallographic symmetry group was  
161 confirmed with Pointless [16] and reflections were merged with Aimless [17]. The data were phased  
162 by molecular placement using Phaser, with a decamer of Rru\_EncFtn (PDB ID: 5DA5) used as the  
163 search model [1]. This has 58 and 22 % sequence identity to the Hoch\_EncFtn and Pfc\_EncFtn  
164 respectively. The sequences were aligned with the 5DA5 protein sequence using ClustalOmega and  
165 the alignment was used to edit the search model to match the target sequence using CHAINSAW  
166 [18]. The crystallographic models were rebuilt using phenix.autobuild [19] and subsequently refined



167 using phenix.refine [20] with cycles of manual model building in Coot [21]. The model quality was  
168 assessed using MolProbity [22]. All structural figures were generated using PyMOL  
169 ([www.pymol.org](http://www.pymol.org)). X-ray data collection and refinement statistics are shown in Table 1.

### 170 ***Sequence alignment and depiction***

171 The protein sequences for Hoch\_3836 and the encapsulated ferritin domain of Pfc\_05175 were  
172 aligned against Rru\_A0973 using Clustal Omega [23] and rendered using ESPript 3.0 [24].

### 173 ***Mass spectrometry***

174 All mass spectrometry (MS) experiments were performed on a Synapt G2 ion-mobility equipped Q-  
175 ToF instrument (Waters Corp., Manchester, UK). LC-MS experiments were performed using an  
176 Acquity UPLC equipped with a reverse phase C4 Aeris Widepore 50 × 2.1 mm HPLC column  
177 (Phenomenex, CA, USA) and a gradient of 5–95% acetonitrile (0.1% formic acid) over 10 minutes  
178 was employed. For LC-MS, samples were typically analysed at 5 µM, and data analysis was  
179 performed using MassLynx v4.1 and MaxEnt deconvolution. For native MS analysis, all protein  
180 samples were buffer exchanged into 100 mM ammonium acetate (pH 8.0, or pH 5.0) using Micro  
181 Biospin Chromatography Columns (Bio-Rad, UK) prior to analysis and the resulting protein samples  
182 were analysed at a typical final concentration of ~5 µM (oligomer concentration). For native MS  
183 ionization, nano-ESI was employed using a nanomate nanoelectrospray infusion robot (Advion  
184 Biosciences, Ithaca, NY). Instrument parameters were tuned to preserve non-covalent protein  
185 complexes and were consistent for the analysis of all protein homologues. After the native MS  
186 optimization, parameters were: nanoelectrospray voltage 1.60 kV; sample cone 100 V; extractor  
187 cone 0 V; trap collision voltage 4 V; source temperature 60 °C; and source backing pressure 6.0  
188 mbar.

### 189 ***ICP-MS***

190 Inductively coupled plasma mass spectrometry experiments were performed on samples of Rru\_His,  
191 Hoch\_His, and Pfc\_His from size-exclusion chromatography experiments and Rru\_StrepII,  
192 Hoch\_StrepII, and Pfc\_StrepII from the affinity chromatography purification step as described  
193 previously [1].

194

## 195 **Results**

### 196 ***Purification of encapsulated ferritins from H. ochraceum and P. furiosus***

197 The encapsulated ferritins from *H. ochraceum* and *P. furiosus* share 18 % amino acid sequence  
198 identity with each other, and 58 % and 22 % with the *R. rubrum* EncFtn (respectively referred to as  
199 Hoch\_EncFtn, Pfc\_EncFtn, and Rru\_EncFtn herein). Residues shown to be in the ferroxidase centre  
200 of the Rru\_EncFtn protein are strictly conserved in the Hoch\_EncFtn and Pfc\_EncFtn proteins, with  
201 secondary metal binding sites conserved in Hoch\_EncFtn, but not in Pfc\_EncFtn (Fig. S3).

202 To explore the structure and function of encapsulated ferritins from different species, we produced  
203 examples of this protein family from *H. ochraceum* and *P. furiosus* as truncated variants, lacking the  
204 C-terminal encapsulin localization sequence, by heterologous expression in *Escherichia coli*. The *H.*  
205 *ochraceum* EncFtn was produced as a C-terminal His-tagged variant, C-terminal StrepII-tagged  
206 variant, and an untagged variant comprising residues 1-98 of the native polypeptide. In *P. furiosus*  
207 the encapsulated ferritin forms a single contiguous polypeptide with the encapsulin shell protein;  
208 therefore, a truncated version with residues 1-99 encompassing just the EncFtn domain was  
209 produced as both a C-terminal His-tagged variant, a C-terminal StrepII-tagged variant, and an  
210 untagged variant. Purity and yield issues with untagged proteins were behind the rational of using  
211 tagged-variants. His-tagged variants were produced for mass-spectrometry analysis, whereas C-  
212 terminal StrepII-tagged variants were used in the enzymatic assay where the presence of the His-  
213 tag could have interfered with metal binding and catalysis. Native untagged proteins were used for  
214 protein crystallography as, after several attempts, only these variants produced crystals suitable for  
215 X-ray diffraction. Average neutral masses were obtained for each homologue by liquid  
216 chromatography mass spectrometry (Table S5). These all agree with the predicted masses of each  
217 protein and revealed that some of the variants lacked full processing of the initiating methionine.

218 To interrogate the behaviour of the EncFtn homologues in solution, both the His-tagged and StrepII-  
219 tagged variants were subjected to S200 size-exclusion chromatography, calibrated with standards  
220 of known molecular weight, and followed by SDS-PAGE analysis (Fig. 1, Table S6, and Fig. S4).  
221 Hoch\_His eluted as three peaks of increasing area: a small peak at ~70 ml consistent with a decamer

222 oligomer; a peak at 81.6 ml consistent with a tetramer; and one at 87.6 ml corresponding to the  
223 dimer fraction. Pfc\_His eluted as a single peak at 64 ml, which has a slightly larger apparent size  
224 than the decamer fraction of Rru\_EncFtn (Fig. 1A). When subjected to SDS-PAGE the Hoch\_His  
225 peak fractions were partially resistant to SDS and heat-induced denaturation, presenting bands at  
226 the approximate molecular weight of a monomer and dimer species (Fig. S4A); the Pfc\_His peak  
227 fractions were almost fully resistant to SDS and heat denaturation with the majority of protein  
228 appearing as a band with an apparent molecular weight greater than that of a decamer, with a small  
229 proportion of monomer (Fig. S4B). Bands corresponding to dimer and monomer states were  
230 observed with Rru\_His variant (Fig. S4C). The StrepII-tagged variants of the proteins behaved  
231 slightly differently in solution (Fig. 1B); Hoch\_StrepII eluted as a monomer; while the Pfc\_StrepII had  
232 a major decamer peak with two additional peaks consistent with higher-order aggregation, such as  
233 dimers of decamers and trimers of decamers. The Rru\_StrepII protein eluted primarily as a decamer.  
234 Their appearance on SDS-PAGE gels was almost identical to the His-variants, with the appearance  
235 of some tetramer in the Pfc\_StrepII fractions (Fig. S4D/E/F).

### 236 ***Native Mass spectrometry analysis***

237 In order to further understand the differences seen in the solution-phase oligomerization states of  
238 the EncFtn homologues, native mass spectrometry was performed on the His-tagged variant of each  
239 homologue. As previously reported [1], the decameric assembly of iron-bound Rru\_EncFtn can be  
240 successfully detected using this technique. Under native MS conditions (at pH 8.0), Rru\_EncFtn  
241 displays a narrow charge state distribution consistent with the 22+ to 25+ charge state of the protein  
242 decamer (Fig. 2A, pink circles). In addition to the decamer, a minor species is observed which is  
243 consistent with the iron-free Rru\_EncFtn monomer (+6 and +7) (Fig. 2A, blue circles).

244 In a similar manner to Rru\_EncFtn, native MS analysis of Pfc\_EncFtn demonstrates charge state  
245 distributions consistent with a decameric assembly (+23 to +26) (Fig. 2B, pink circles). Interestingly,  
246 the decameric charge state distribution is elongated (Fig. 2B, \*) and low abundance (27+ to 31+)  
247 charge states are also observed. The elongated charge state distribution is only observed in  
248 Pfc\_EncFtn, and we attribute its presence to the ability of the solvent-exposed affinity tag to readily  
249 protonate in solution. Similar to the observations from Rru\_EncFtn, a charge state distribution

250 consistent with iron-free Pfc\_EncFtn monomer (+5 to +17) is also observed (Fig. 2B, blue circles).  
251 In contrast, native MS analysis of Hoch\_EncFtn does not reveal a major decamer species. Instead  
252 a series of oligomerization states are observed: the major species is a dimer (+9 to +12) (Fig. 2C,  
253 green circles); in addition tetramer (+13 to +16), hexamer (17+ and 18+) and decamer (23+ to 25+),  
254 and a small amount of monomer (+7 to +12) gas phase oligomerization states are all clearly  
255 observed (Fig. 2C, purple circles, orange circles, pink circles, and blue circles respectively). This  
256 observation is consistent with the multiple broad peaks obtained during size-exclusion  
257 chromatography (Fig. 1).

258 These data suggest that, under our experimental conditions, multiple oligomeric assemblies of Hoch  
259 protein exist in both the solution and gas phase. The observation of even-numbered oligomerization  
260 states (i.e. dimer, tetramer and hexamer) suggests that one of the two dimer interfaces is partially  
261 unstable, and the protein exists as an equilibrium of dimers and higher order multiples of dimers.

### 262 ***Crystal structures of Hoch and Pfc Encapsulated ferritins***

263 To explore the structure of the EncFtn homologues, crystals of native Hoch\_EncFtn and Pfc\_EncFtn  
264 were produced by standard crystallization screening methods. Diffraction data were collected at  
265 Diamond Light Source and the crystal structures of the Hoch\_EncFtn and Pfc\_EncFtn proteins were  
266 determined by molecular replacement using a decamer of the Rru\_EncFtn (PDB ID: 5DA5) as the  
267 search model [1]. Data collection and refinement statistics are shown in Table 1.

268 The structure of Hoch\_EncFtn was refined at 2.06 Å resolution and contained a decamer in the  
269 asymmetric unit with visible electron density for residues 6 – 96 in each chain (Fig. 3A). Pfc\_EnFtn  
270 was refined at 2.03 Å resolution and contained three decamers in the asymmetric unit, with visible  
271 electron density for residues 2-98 in each chain (Fig. 3B). The overall architecture of both structures  
272 mirrors the annular decamer seen in the structure of Rru\_EncFtn (Fig. 3C). The electrostatic surfaces  
273 of these proteins display similar features to Rru\_EncFtn, with negatively charged patches around  
274 the circumference that correspond to the exterior metal binding sites seen on Rru\_EncFtn, and a  
275 negatively charged tunnel at the centre of the decamer corresponding to the interior metal binding  
276 site (Fig. S5).

277 The monomers of Hoch\_EncFtn and Pfc\_EncFtn superimpose with an RMSD of 1.21 Å over 74 C $\alpha$   
278 atoms. Hoch\_EncFtn superimposes on Rru\_EncFtn with an RMSD of 0.47 Å over 91 C $\alpha$  atoms,  
279 while Pfc\_EncFtn superimposes with an RMSD of 1 Å over 71 C $\alpha$  atoms. While the Hoch\_EncFtn  
280 and Rru\_EncFtn structures are almost identical, the Pfc\_EncFtn structure presents several key  
281 differences to these two proteins. At the N-terminus of Pfc\_EncFtn, there is visible electron density  
282 from Gly2, whereas the chains of both Hoch\_EncFtn and Rru\_EncFtn are not visible until residue  
283 Gln6 and Ser7 respectively. The additional structured residues in Pfc\_EncFtn form an extended loop  
284 (Fig. 4), which lies in the central channel of the physiologically active decamer and forms a rigid  
285 constriction when compared to the Hoch\_EncFtn and Rru\_EncFtn structures (Fig. 3B). The C-  
286 terminal  $\alpha$ 3 helix of Pfc\_EncFtn has two additional turns when compared to the other structures and  
287 is shifted by 25° relative to  $\alpha$ 2 (Fig. 4B/C); this extends its interaction with the neighbouring dimer.  
288 (Fig. 3B).

289 The main interaction surfaces that make up the decameric arrangement in the proteins correspond  
290 to the ferroxidase centre dimer (FOC) and the non-ferroxidase dimer (non-FOC) interfaces (Fig.  
291 3B/C). Analysis of the extent of these surfaces with PISA [25] gives a buried surface of 1186 Å<sup>2</sup> for  
292 the Hoch\_EncFtn FOC interface, with 8 hydrogen bonds and 16 salt bridges; and 1712 Å<sup>2</sup> in  
293 Pfc\_EncFtn, with 14 hydrogen bonds and 6 salt bridges (Fig S6). While Hoch\_EncFtn buries roughly  
294 the same surface area in its FOC interface as Rru\_EncFtn FOC (1267 Å<sup>2</sup>), the latter has only 2  
295 hydrogen bonds and 6 salt bridges; the additional stabilization of this interface in Hoch\_EncFtn is  
296 likely related to the environmental niche of *Haliangium ochraceum*, as proteins from halophilic  
297 organisms tend to have an increased number of salt bridges when compared to those from  
298 mesophiles [26]. The Pfc\_EncFtn FOC interface has fourteen hydrogen bonds and six salt bridges;  
299 this significant increase in hydrogen bonding over the Rru\_EncFtn protein is likely to be a  
300 consequence of the hyperthermophilic nature of *Pyrococcus furiosus*. The non-FOC interface for  
301 Hoch\_EncFtn buries 2338 Å<sup>2</sup>, which is similar to the 2468 Å<sup>2</sup> buried in this region in Rru\_EncFtn;  
302 however, there are 18 hydrogen bonds compared to 16 in Rru\_EncFtn, and 5 salt bridges compared  
303 to 16 in Rru\_EncFtn. These differences are due to a higher proportion of buried hydrophobic residues  
304 in the Hoch\_EncFtn interface. The non-FOC interface in the Pfc\_EncFtn is less extensive than either

305 of the other two structures at 1793 Å<sup>2</sup> with 19 hydrogen bonds and 19 salt bridges. The extended  
306 structured loop at the N-terminus and shifted  $\alpha$ 3 helix form one hydrogen bond each to the monomer  
307 next to their partner in the FOC interface, to bury an additional 586 Å<sup>2</sup> of surface area (Fig S6). Taken  
308 together, these two interfaces bury about the same surface area as the non-FOC interfaces of both  
309 Rru\_EncFtn and Hoch\_EncFtn. The extended interaction surfaces in the Pfc\_EncFtn potentially act  
310 as a girdle around the decamer, further stabilizing it at high temperatures.

311 The residues in the iron binding site of the FOC interface are conserved in the Hoch\_EncFtn and  
312 Pfc\_EncFtn structures (Fig. 5). The Pfc\_EncFtn structure shows clear anomalous difference density  
313 in data collected close to the iron edge at 1.74 Å (Fig. S7; therefore, a dinuclear iron centre was  
314 modelled into the FOC of this structure (Fig. 5). The metal coordination in Pfc\_EncFtn is identical to  
315 that seen in Rru\_EncFtn, with glutamic acid carboxyl oxygen to iron coordination distances of 2.1 Å,  
316 and histidine nitrogen to iron distances of 2.2 Å. The electron density in the FOC interface of the  
317 Hoch\_EncFtn crystal does not contain any peaks or coordinated metal ions (Fig. S7). Given the  
318 importance of the histidine residue (His64) for iron coordination [1] and the fact that the protein  
319 crystallized in a buffer at pH 5.5, this histidine residue is likely to be around 70 % protonated and  
320 would be unable to coordinate iron in this state, thus explaining the absence of iron in this site. In  
321 the absence of iron in the Hoch\_EncFtn structure, the side-chain of Glu31 is flipped 180° and is  
322 within hydrogen bonding distance of Tyr38 from the partner chain, presumably stabilizing the apo-  
323 form of this interface (Fig. 5A).

324 The secondary metal coordination sites seen in the structure of Rru\_EncFtn are fully conserved in  
325 Hoch\_EncFtn and only partially so in Pfc\_EncFtn. The metal binding site at the centre of the  
326 decameric ring comprises Glu30/Glu33 in Hoch\_EncFtn and Ala31/Asp34 in Pfc\_EncFtn. Neither  
327 structure has any coordinated metal ions in this site (Fig. 5B).

328 The side-chains of the glutamic acid residues (Glu31/Glu34 in Rru\_EncFtn numbering) are shifted  
329 when compared to those in Rru\_EncFtn; this could be linked to the absence of a metal ion. The  
330 external metal binding site of Hoch\_EncFtn is identical to the Rru\_EncFtn site, while the Pfc\_EncFtn  
331 has a glutamic acid in place of a histidine and alanine in place of a glutamic acid in this site.

332 Given the observation that a decameric form of Hoch\_EncFtn was obtained in crystals at pH 5.5, the  
333 influence of pH on protein oligomerization was investigated using native MS. Experiments were  
334 performed in pH 5.5 ammonium acetate, and under these acidic conditions MS analysis reveals a  
335 substantial increase in the abundance of the decameric species (21+ to 25+) (Fig. S8), similar to the  
336 level seen for Pfc\_EncFtn and Rru\_EncFtn. The lower order oligomerization states, present at pH  
337 8.0, are significantly reduced in abundance and only dimer (9+ and 10+) and tetramer (14+ and 15+)  
338 minor species are observed (Fig. S8, green and purple circles respectively). Taken together, our  
339 native MS observations suggest that a stable Hoch EncFtn dimer is readily formed irrespective of  
340 pH; and under acidic conditions, Hoch\_EncFtn dimers favour assembly into the higher order  
341 pentamer-of-dimers annular structure which is characteristic of this class of protein.

#### 342 ***Ferroxidase activity***

343 Given the absolute conservation of the FOC residues in Hoch\_EncFtn, Pfc\_EncFtn and Rru\_EncFtn,  
344 the ferroxidase activity of the EncFtn homologues was tested to determine if they were indeed active  
345 as ferroxidase enzymes. Encapsulated ferritin StrepII-tagged variants were assayed for their  
346 ferroxidase activity by following progress curves for iron oxidation at 315 nm at 20 °C. Each of the  
347 proteins displayed similar activity profiles, with some small differences in the shape of the progress  
348 curves. Hoch\_EncFtn exhibits a higher initial rate than the other homologues (Fig. 6). Overall these  
349 data confirm the ferroxidase activity of the EncFtn family across different species from distinct  
350 environmental niches.

351 The metal content of the purified protein fractions used for enzymatic assays was determined by  
352 inductively coupled plasma mass spectrometry (Table S7). Iron levels determined in StrepII-tagged  
353 monomeric Hoch\_EncFtn variants and StrepII-tagged decameric Pfc\_EncFtn and Rru\_EncFtn  
354 variants show an iron to protein ratio consistent with 40-80 % occupancy of the ferroxidase centre,  
355 assuming all of the iron is located within this site. A ~50 % occupancy of the ferroxidase centre was  
356 also observed with the His-tagged EncFtn variants which were used in the mass-spectrometry  
357 analysis.

358 Significant amounts of zinc were copurified with all protein samples in this study, with varying levels  
359 detected in the forms with different tags. Zinc is known to strongly inhibit the ferroxidase activity of

360 ferritin family proteins via competitive binding to the ferroxidase centre [27]. Given the structural  
361 differences between encapsulated ferritins and the classical ferritins, and the differences in  
362 secondary metal-binding sites displayed by Pfc\_EncFtn, the inhibitory effect of zinc on the EncFtn  
363 homologues was tested by performing the ferroxidase assays in the presence of increasing  
364 concentrations of zinc. The results show that increasing zinc concentrations lead to a decrease in  
365 the slope and final level of ferroxidase progress curves for all of the EncFtn variants, with a maximum  
366 inhibition seen with ~ 40-100  $\mu$ M Zn (Fig. S9). These data were fitted using a nonlinear regression  
367 with a dose-response model with three parameters, where the response (zero-subtracted end-point  
368 absorbance at 315 nm) was the average of three replicates per condition (Fig. 7). The calculated  
369 IC<sub>50</sub> values for zinc inhibition of the three EncFtn variants (Table S8) show significant differences,  
370 with the Rru\_EncFtn showing the lowest, and Hoch\_EncFtn the highest IC<sub>50</sub> values. The lower  
371 susceptibility of the Hoch\_EncFtn to zinc dependent inhibition could be a consequence of a higher  
372 level of ferroxidase activity, or structural differences that influence metal binding and discrimination.

373

374

375

376



377 **Discussion**

378 The recently published structural and functional analysis of the *R. rubrum* encapsulated ferritin  
379 system presented a new functional organization for iron mineralization by ferritin-like proteins, with  
380 the four-helix bundle ferritin-like fold formed through the interaction of EncFtn subunits to form a  
381 functional ferroxidase centre [1]. The open decameric structure of the EncFtn protein is not  
382 competent to store iron in mineral form; instead, the interaction with, and sequestration within, the  
383 encapsulin nanocage provides a functional and high-capacity iron storage system [3,4]. To  
384 understand whether the structural organization of the EncFtn family is conserved across  
385 microorganisms with different environmental niches and distinct encapsulin geometries, we  
386 determined the structure and biochemical properties of EncFtn proteins from *H. ochraceum* and *P.*  
387 *furiosus*.

388 *P. furiosus* is a hyperthermophilic Euryarchaeota and its encapsulin was the first to be characterized;  
389 however, it was initially mis-annotated as a non-functional virus-like particle [13]. The *P. furiosus*  
390 encapsulin forms a contiguous polypeptide chain with an N-terminal EncFtn domain appended to it  
391 and assembles into a 180 subunit T=3 capsid. This archaeal arrangement is distinct to the bacterial  
392 EncFtn/encapsulin systems, which are usually encoded in a two-gene operon with the EncFtn  
393 upstream of the encapsulin, and with a short C-terminal encapsulation sequence peptide appended  
394 to the encoded EncFtn protein [5, 10]. It is not clear whether the genomic arrangement of the bacterial  
395 EncFtn/encapsulin systems arose separately, or by horizontal gene transfer from archaea followed  
396 by mutation of the single-reading frame into two, along with the mutation of the T=3 form of the  
397 encapsulin to the T=1 form found in the bacterial EncFtn encapsulins.

398 The published crystal structure of the *P. furiosus* encapsulin lacks any electron density for  
399 the EncFtn domain, implying that this domain is mobile within the encapsulin nanocage even though  
400 it is contiguous with and tethered to the encapsulin protein [13]. Our analysis focused on the isolated  
401 *P. furiosus* EncFtn domain, which forms a decamer in solution, the gas phase, and in crystals. This  
402 domain is partially resistant to thermal and SDS induced denaturation, which is in accord with the  
403 extreme temperatures endured by the host organism in its volcanic niche.

404 The current model for the organization of bacterial EncFtn proteins within encapsulin nanocages  
405 places the decamers at the pentameric vertices of the T=1 capsid [1,4] with the encapsulation  
406 sequences of five subunits captured by clefts on the interior surface of the penton of the encapsulin  
407 shell. The encapsulation sequences of the other five subunits in the decamer are disengaged and  
408 free within the interior of the capsid. No evidence is available on the strength of the interaction  
409 between the capsid and the EncFtn protein; however, the presence of clear electron density for some  
410 of the encapsulation sequence in the *T. maritima* encapsulin structure implies that the interaction is  
411 relatively stable, and this is enhanced by an avidity mechanism with multiple encapsulation  
412 sequences engaged by subunits at the pentameric vertex [4]. In the archaeal systems the EncFtn  
413 and encapsulin domains are a contiguous polypeptide, with the EncFtn domain tethered to the  
414 interior of the capsid. The T=3 geometry of the *P. furiosus* encapsulin has 180 subunits, with 12  
415 penton units and 20 hexons. Given the structural and biochemical conservation of the decameric  
416 EncFtn protein, it is likely that this arrangement is found within the T=3 as well as T=1 capsids. It is  
417 not clear how the decamer could be formed from tethered subunits unless the EncFtn domains found  
418 in hexons have enough flexibility in the linker between domains to engage with partners in adjacent  
419 pentons. With full engagement at the pentons, this would leave 60 'free' EncFtn domains within the  
420 capsid. This observation, coupled with our solution and gas phase experiments, indicates that the  
421 quaternary structure of EncFtn proteins is dynamic and that they can exist in equilibrium between  
422 monomers/dimers and higher order multiples of dimers.

423 The dynamic nature of EncFtn proteins is highlighted in our solution and gas phase analyses  
424 of the *H. ochraceum* EncFtn. Despite high sequence identity and the conservation of key residues  
425 between it and the *R. rubrum* EncFtn, this protein is less prone to multimerization in solution and  
426 displays a greater range of oligomerization intermediates than both the *R. rubrum* and *P. furiosus*  
427 EncFtn proteins in the gas phase. The presence of the conserved EncFtn decamer quaternary  
428 structure in the crystal highlights the conservation of this architecture. The absence of metal ions in  
429 the crystal structure, which was formed at pH 5.5, indicated that the quaternary structure can be  
430 induced by both metal binding, as was shown in solution for the *R. rubrum* EncFtn [1], and changes  
431 in pH, presumably through the protonation of the conserved histidine at low pH and the formation of  
432 stabilizing hydrogen bonds by residues normally involved in the formation of the FOC.

433 Analysis of the structure and sequence of the *H. ochraceum* EncFtn indicates that the dimerization  
434 interfaces are less extensive than the *R. rubrum* EncFtn interfaces and are discontinuous. This leads  
435 to lower binding energies for both of the interfaces when compared to both *R. rubrum* and *P. furiosus*,  
436 and this could explain the differences in stability seen in solution and the gas phase.

437 We show here that the three proteins in this study exhibit comparable ferroxidase activities. This  
438 indicates that they were purified in a functional state. Previous reports show that ferritins are  
439 susceptible to inhibition by Zn(II) ions [27], which is also the case for the EncFtn family as  
440 demonstrated in this study. In the experimental conditions used in our study, the *H. ochraceum*  
441 EncFtn was slightly more active than the other proteins and less susceptible to inhibition by zinc.  
442 This may be a consequence of the more dynamic nature of this homologue, as seen in solution and  
443 the gas phase. The precise mode of catalysis for ferritins is a subject of some debate and key  
444 questions as to whether the iron ions engaged within the ferroxidase centre are labile, or act as a  
445 stable prosthetic centre; and whether the two iron ions move in concert are the subject of some  
446 controversies in the field [28,29]. Our study does not aim to address these controversies, but we do  
447 note that the location of the conserved FOC and secondary metal binding sites at a dimer interface  
448 and the dynamic nature of EncFtn oligomerization may indicate a distinct mechanism of iron  
449 oxidation and transfer to minerals when compared to the classical ferritins, thus adding a new level  
450 of complexity and debate to the field. It must also be noted that the activity of EncFtn proteins occurs  
451 within the privileged environment of an encapsulin shell, which adds an additional level of complexity  
452 to the study of their catalysis.

453 Analysis of the sequence alignment (Fig. S3) highlights the absence of conserved residues found in  
454 the putative metal ion entry site found in the other EncFtn homologues. Our observation that Pfc  
455 EncFtn displays ferroxidase activity highlights that conservation of this site is not a prerequisite for  
456 catalysis. However, it is clear that Pfc\_EncFtn has the lowest enzymatic activity of the three  
457 homologues, it may be that that the acidic residues found in this location attract iron ions and channel  
458 them to the FOC. Their absence in Pfc\_EncFtn implies that metal ions reach its FOC simply by  
459 diffusion, resulting in a slower Fe(II)/Fe(III) turn-over and hence a reduction in enzyme activity. It  
460 would be interesting to apply a mutagenesis approach to further explore the role of these proposed

461 entry site residues on the ferroxidase activity. The modest catalytic activity displayed by Pfc\_EncFtn  
462 could also be interpreted by considering that *P. furiosus* achieves optimal growth at ~ 100 °C,  
463 whereas enzymatic experiments were conducted at room temperature to allow the comparison of  
464 activities.

465 Further study will shed light on the role of the different dimerization interfaces on the stability of the  
466 EncFtn decamer; and the role of the secondary metal binding sites on catalysis, metal selectivity,  
467 and catalytic inhibition by competing metal ions.

468

469 **Author Contributions**

470 DH, JMW and DC conceived the study. DH produced the native and His-tagged constructs used in  
471 the study. LRT produced the DNA parts and assembled the StrepII-tagged variants of the EncFtn  
472 proteins. DH, CP, JR, ZM and JMW produced recombinant proteins used in the study. DH and JMW  
473 determined and refined the crystal structures. CP performed biochemical assays shown in Figures  
474 6/7/S9. JR and DC performed mass spectrometry experiments shown in Figures 2 and S8. CLM  
475 provided technical assistance and contributed to data collection for MS experiments. KJW and ET  
476 performed ICP-MS experiments shown in Table S7. All authors contributed to data analysis and  
477 preparation of the manuscript.

478 **Funding**

479 This work was supported a Royal Society Research Grant awarded to JMW (RG130585) and a  
480 BBSRC New Investigator Grant to JMW and DJC (BB/N005570/1). JMW is funded by Newcastle  
481 University. DJC and JR are funded by the University of Edinburgh. JR is funded by a BBSRC EastBio  
482 DTP studentship (BB/M010996/1). DH was funded by the China Scholarship Council. LRT was  
483 funded by a BBSRC EastBio DTP Studentship (BB/M010996/1). KJW and ET were funded by the  
484 Wellcome Trust and Royal Society through a Sir Henry Dale Fellowship awarded to KJW  
485 (098375/Z/12/Z).

486 **Competing Interests**

487 The authors declare that there are no competing interests.

488 **Acknowledgements**

489 The authors would like to thank Diamond Light Source for beamtime (proposal mx9487), and the  
490 staff of beamlines I04 and I24 for assistance with crystal testing and data collection.

491 We would like to thank Prof Dominic Campopiano and Dr Elisabeth Lowe for their critical reading of  
492 this manuscript and helpful discussions.

493

494

495 **References**

- 496 1 He, D., Hughes, S., Vanden-Hehir, S., Georgiev, A., Altenbach, K., Tarrant, E., Mackay, C. L.  
497 L., Waldron, K. J. K. J., Clarke, D. J. D. J. and Marles-Wright, J. (2016) Structural  
498 characterization of encapsulated ferritin provides insight into iron storage in bacterial  
499 nanocompartments. *Elife* **5**, e18972.
- 500 2 Andrews, S. C. (2010) The Ferritin-like superfamily: Evolution of the biological iron storeman  
501 from a rubrerythrin-like ancestor. *Biochim. Biophys. Acta*, Elsevier B.V. **1800**, 691–705.
- 502 3 McHugh, C. A., Fontana, J., Nemecek, D., Cheng, N., Aksyuk, A. A., Heymann, J. B., Winkler,  
503 D. C., Lam, A. S., Wall, J. S., Steven, A. C., et al. (2014) A virus capsid - like  
504 nanocompartment that stores iron and protects bacteria from oxidative stress. *EMBO J.*,  
505 *EMBO Press* **33**, 1896–1911.
- 506 4 Sutter, M., Boehringer, D., Gutmann, S., Günther, S., Prangishvili, D., Loessner, M. J., Stetter,  
507 K. O., Weber-Ban, E. and Ban, N. (2008) Structural basis of enzyme encapsulation into a  
508 bacterial nanocompartment. *Nat. Struct. Mol. Biol.*, Nature Publishing Group **15**, 939–947.
- 509 5 Giessen, T. W. and Silver, P. A. (2017) Widespread distribution of encapsulin  
510 nanocompartments reveals functional diversity. *Nat. Microbiol.*, Nature Publishing Group **2**,  
511 17029.
- 512 6 Crow, A., Lawson, T. L., Lewin, A., Moore, G. R. and Le Brun, N. E. (2009) Structural basis  
513 for iron mineralization by bacterioferritin. *J. Am. Chem. Soc.*, American Chemical Society **131**,  
514 6808–13.
- 515 7 Bakker, G. R. and Boyer, R. F. (1986) Iron incorporation into apoferritin. The role of apoferritin  
516 as a ferroxidase. *J. Biol. Chem.* **261**, 13182–13185.
- 517 8 Bradley, J. M., Moore, G. R. and Le Brun, N. E. (2014) Mechanisms of iron mineralization in  
518 ferritins: one size does not fit all. *J. Biol. Inorg. Chem.* **19**, 775–85.
- 519 9 Chasteen, N. D. and Harrison, P. M. (1999) Mineralization in ferritin: an efficient means of iron  
520 storage. *J. Struct. Biol.* **126**, 182–94.
- 521 10 Sutter, M., Boehringer, D., Gutmann, S., Günther, S., Prangishvili, D., Loessner, M. J., Stetter,

- 522 K. O., Weber-Ban, E. and Ban, N. (2008) Structural basis of enzyme encapsulation into a  
523 bacterial nanocompartment. *Nat. Struct. Mol. Biol.* **15**, 939–947.
- 524 11 Snijder, J., Kononova, O., Barbu, I. M., Uetrecht, C., Rurup, W. F., Burnley, R. J., Koay, M. S.  
525 T., Cornelissen, J. J. L. M., Roos, W. H., Barsegov, V., et al. (2016) Assembly and Mechanical  
526 Properties of the Cargo-Free and Cargo-Loaded Bacterial Nanocompartment Encapsulin.  
527 *Biomacromolecules* **17**, 2522–9.
- 528 12 Rurup, W. F., Snijder, J., Koay, M. S. T., Heck, A. J. R. and Cornelissen, J. J. L. M. (2014)  
529 Self-sorting of foreign proteins in a bacterial nanocompartment. *J. Am. Chem. Soc.*, American  
530 Chemical Society **136**, 3828–32.
- 531 13 Akita, F., Chong, K. T., Tanaka, H., Yamashita, E., Miyazaki, N., Nakaishi, Y., Suzuki, M.,  
532 Namba, K., Ono, Y., Tsukihara, T., et al. (2007) The crystal structure of a virus-like particle  
533 from the hyperthermophilic archaeon *Pyrococcus furiosus* provides insight into the evolution  
534 of viruses. *J. Mol. Biol.* **368**, 1469–83.
- 535 14 Iverson, S. V., Haddock, T. L., Beal, J. and Densmore, D. M. (2016) CIDAR MoClo: Improved  
536 MoClo Assembly Standard and New *E. coli* Part Library Enable Rapid Combinatorial Design  
537 for Synthetic and Traditional Biology. *ACS Synth. Biol.*, American Chemical Society **5**, 99–  
538 103.
- 539 15 Kabsch, W. (2010) Integration, scaling, space-group assignment and post-refinement. *Acta*  
540 *Crystallogr. Sect. D Biol. Crystallogr.*, International Union of Crystallography **66**, 133–144.
- 541 16 Evans, P. R. (2011) An introduction to data reduction: space-group determination, scaling and  
542 intensity statistics. *Acta Crystallogr. D. Biol. Crystallogr.* **67**, 282–92.
- 543 17 Evans, P. (2006) Scaling and assessment of data quality. In *Acta Crystallographica Section*  
544 *D: Biological Crystallography*, pp 72–82, International Union of Crystallography.
- 545 18 Stein, N. (2008) CHAINSAW: A program for mutating pdb files used as templates in molecular  
546 replacement. *J. Appl. Crystallogr.* **41**, 641–643.
- 547 19 Terwilliger, T. C., Grosse-Kunstleve, R. W., Afonine, P. V., Moriarty, N. W., Zwart, P. H., Hung,  
548 L. W., Read, R. J. and Adams, P. D. (2007) Iterative model building, structure refinement and

- 549 density modification with the PHENIX AutoBuild wizard. *Acta Crystallogr. Sect. D Biol.*  
550 *Crystallogr.*, International Union of Crystallography **64**, 61–69.
- 551 20 Afonine, P. V., Grosse-Kunstleve, R. W., Echols, N., Headd, J. J., Moriarty, N. W.,  
552 Mustyakimov, M., Terwilliger, T. C., Urzhumtsev, A., Zwart, P. H. and Adams, P. D. (2012)  
553 Towards automated crystallographic structure refinement with phenix.refine. *Acta Crystallogr.*  
554 *Sect. D Biol. Crystallogr.*, International Union of Crystallography **68**, 352–367.
- 555 21 Emsley, P., Lohkamp, B., Scott, W. G. and Cowtan, K. (2010) Features and development of  
556 Coot. *Acta Crystallogr. D. Biol. Crystallogr.* **66**, 486–501.
- 557 22 Chen, V. B., Arendall, W. B., Headd, J. J., Keedy, D. A., Immormino, R. M., Kapral, G. J.,  
558 Murray, L. W., Richardson, J. S. and Richardson, D. C. (2010) MolProbity: all-atom structure  
559 validation for macromolecular crystallography. *Acta Crystallogr. D. Biol. Crystallogr.* **66**, 12–  
560 21.
- 561 23 Sievers, F. and Higgins, D. G. (2014) Clustal Omega, accurate alignment of very large  
562 numbers of sequences. *Methods Mol. Biol.* **1079**, 105–16.
- 563 24 Gouet, P., Robert, X. and Courcelle, E. (2003) ESPript/ENDscript: Extracting and rendering  
564 sequence and 3D information from atomic structures of proteins. *Nucleic Acids Res.* **31**,  
565 3320–3.
- 566 25 Krissinel, E. and Henrick, K. (2007) Inference of macromolecular assemblies from crystalline  
567 state. *J. Mol. Biol.* **372**, 774–97.
- 568 26 DasSarma, S. and DasSarma, P. (2015) Halophiles and their enzymes: negativity put to good  
569 use. *Curr. Opin. Microbiol.* **25**, 120–126.
- 570 27 Pfaffen, S., Abdulqadir, R., Le Brun, N. E. and Murphy, M. E. P. (2013) Mechanism of ferrous  
571 iron binding and oxidation by ferritin from a pennate diatom. *J. Biol. Chem.* **288**, 14917–25.
- 572 28 Ebrahimi, K., Eckhard, B., Hagedoorn, P. and Hagen, W. (2012) The catalytic center of ferritin  
573 regulates iron storage via Fe (II)-Fe (III) displacement. *Nat. Chem. Biol.* **8**, 941–948.
- 574 29 Hagen, W. R., Hagedoorn, P.-L. and Honarmand Ebrahimi, K. (2017) The workings of ferritin:



575 a crossroad of opinions. *Metallomics*, The Royal Society of Chemistry **9**, 595–605.

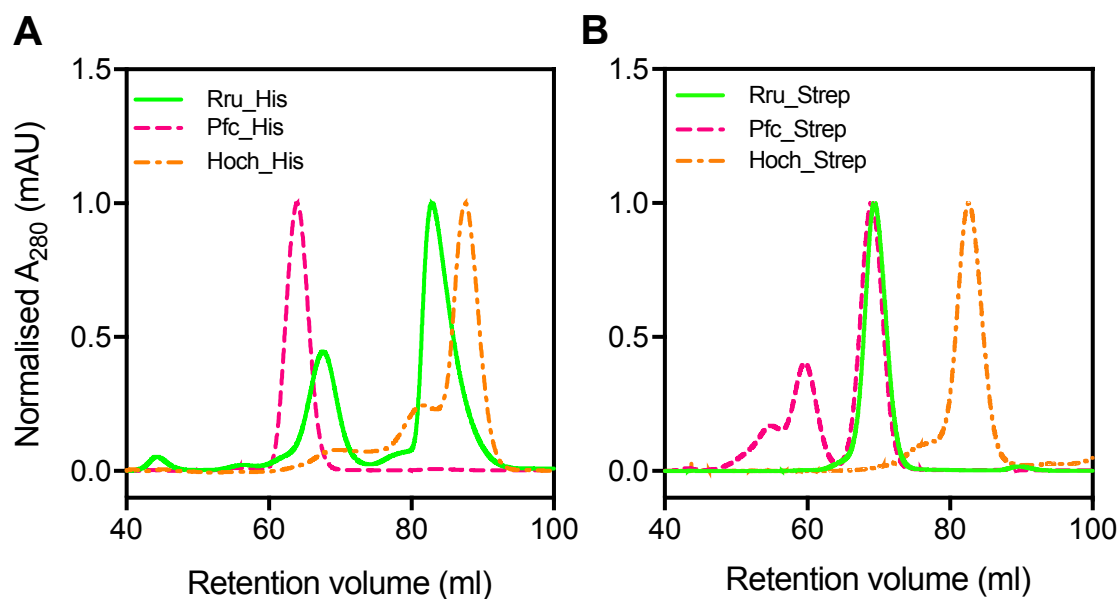
576

577

579 Table 1. X-ray diffraction data collection and refinement statistics.

	Hoch_EncFtn	Pfc_EncFtn*
<b>Data collection</b>		
<b>Wavelength (Å)</b>	1.72	1.74
<b>Resolution range (Å)</b>	47.82 - 2.06 (2.13 - 2.06)	47.19 - 2.03 (2.1 - 2.03)
<b>Space group</b>	C 1 2 1	P 1 21 1
<b>Unit cell (Å)</b> <b>β (°)</b>	91.63, 92.65, 119.29 106.94	99.85, 110.06, 136.27 91.22
<b>Total reflections</b>	30,0549 (27,242)	1,226,338 (112,156)
<b>Unique reflections</b>	57,293 (5,570)	374,905 (36,076)
<b>Multiplicity</b>	5.2 (4.9)	3.3 (3.0)
<b>Completeness (%)</b>	96.3 (94.1)	97.0 (95.4)
<b>Mean I/sigma(I)</b>	10.16 (2.37)	10.48 (4.02)
<b>Wilson B-factor (Å<sup>2</sup>)</b>	31.7	22.8
<b>R<sub>merge</sub> (%)</b>	9.4 (59.6)	8.0 (36.3)
<b>R<sub>meas</sub> (%)</b>	10.5 (66.7)	9.5 (44.1)
<b>R<sub>pim</sub> (%)</b>	4.4 (29.2)	5.2 (24.7)
<b>CC<sub>1/2</sub> (%)</b>	100 (99.9)	99.5 (90.2)
<b>CC* (%)</b>	100 (97.6)	100 (97.4)
<b>Image DOI</b>	10.5281/zenodo.322743	10.5281/zenodo.344797
<b>Refinement</b>		
<b>Reflections used in refinement</b>	57,082 (5,563)	365,581 (36,036)
<b>Reflections used for R-free</b>	2,765 (284)	17,934 (1697)
<b>Rwork (%)</b>	20.1 (29.5)	17.5 (22.3)
<b>Rfree (%)</b>	24.5 (34.5)	20.2 (24.5)
<b>CC(work) (%)</b>	96.4 (92.6)	96.7 (92.3)
<b>CC(free) (%)</b>	93.6 (85.1)	95.3 (90.3)
<b>Non-hydrogen atoms</b>	7,819	25,735
<b>macromolecules</b>	7,650	23,691
<b>ligands</b>	1	30
<b>Water</b>	168	2,014
<b>Protein residues</b>	916	2,922
<b>RMS(bonds) (Å)</b>	0.003	0.002
<b>RMS(angles) (°)</b>	0.46	0.44
<b>Ramachandran</b>		
<b>favoured (%)</b>	98.7	99.9
<b>allowed (%)</b>	1.3	0.10
<b>outliers (%)</b>	0.00	0.00
<b>Rotamer outliers (%)</b>	0.96	0.39
<b>Clashscore</b>	1.20	1.15
<b>Average B-factor (Å<sup>2</sup>)</b>	44.6	29.0
<b>macromolecules</b>	44.6	28.3
<b>ligands</b>	34.7	19.7
<b>solvent</b>	43.7	36.7
<b>PDB ID</b>	5N5F	5N5E

580 \*Anomalous pairs were counted separately for Pfc\_EncFtn, as this model was refined against the split  
581 anomalous data. Statistics for the highest-resolution shell are shown in parentheses.

583 **Figures**

584

585 **Figure 1. Purification of recombinant *R. rubrum*, *H. ochraceum*, and *P. furiosus* EncFtn**586 **proteins.** A, Recombinant His-tagged Hoch\_His, Pfc\_His, and Rru\_His proteins were purified by

587 nickel NTA-affinity chromatography and subjected to analytical size-exclusion chromatography

588 using a Superdex 200 16/60 column (GE Healthcare) equilibrated with 50 mM Tris-HCl, pH 8.0,

589 150 mM NaCl. The peaks near 70 ml correspond to an estimated molecular weight of &gt;130 kDa

590 when compared to calibration standards, consistent with oligomerisation states equal or greater

591 than decameric. The Hoch\_His at around 80 ml corresponds to the 50 kDa tetramer and the peaks

592 near 88 ml correspond to the 31 kDa dimer compared to the standards. B, Recombinant Strep-

593 tagged Hoch\_StrepII, Pfc\_StrepII, and Rru\_StrepII proteins were purified by Strep-Trap column HP

594 (GE Healthcare). Purified samples were applied to a Superdex 200 16/60 column (GE Healthcare)

595 equilibrated with 50 mM Tris-HCl, pH 8.0, 150 mM NaCl in order to observe oligomerization state

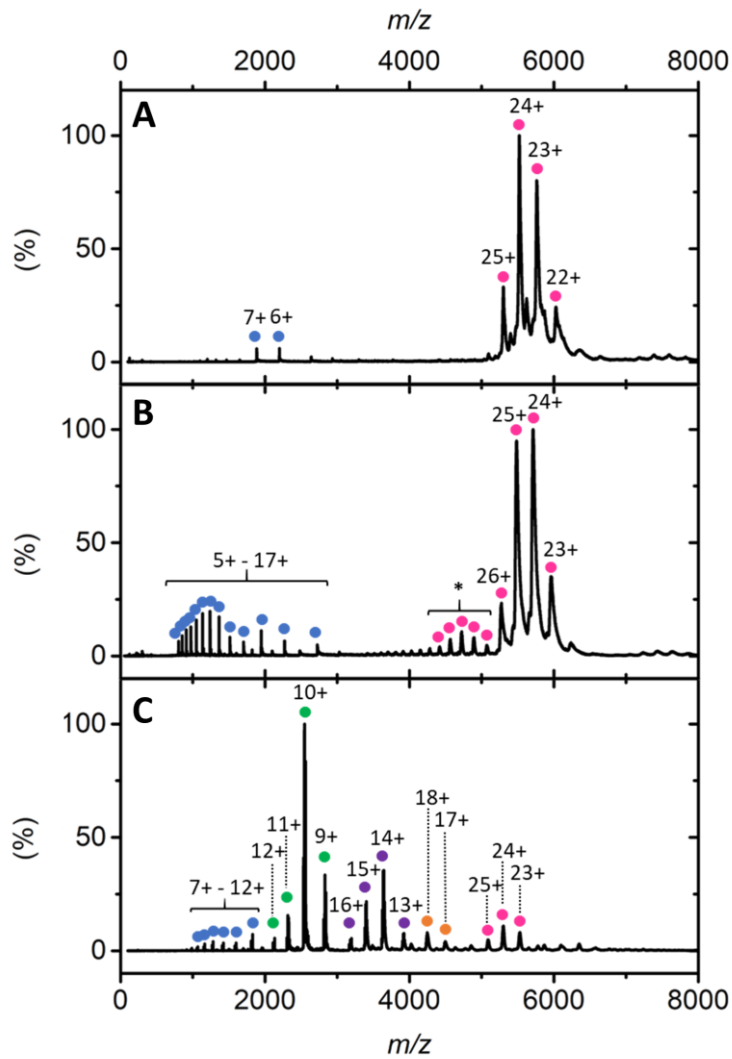
596 in solution. Rru\_StrepII elutes primarily at ~ 70 ml, corresponding to the decamer size. Pfc\_StrepII

597 peaks can be found around 60 ml (~ 24-mer) and at 70 ml (12-mer), whereas Hoch\_StrepII elutes

598 at ~ 83 ml (4-mer). Elution volumes and corresponding oligomerisation states are summarised in

599 Table S6. DOI: 10.6084/m9.figshare.7105907

600



601

602 **Figure 2. Native mass spectrometry of encapsulated ferritin homologues.** Native

603 nanoelectrospray ionization (nESI) mass spectrometry of encapsulated ferritin homologues

604 acquired in 100 mM ammonium acetate (pH 8.0). A: nESI spectrum of Rru\_EncFtn consistent with

605 decameric assembly. The decameric charge state distribution is represented with pink circles and

606 peaks correspond to 22+ to 25+ charge states. Two minor monomer charge states (blue circles, 6+

607 and 7+ charge states) are also observed. B: Native spectrum of Pfc\_EncFtn. Decamer charge

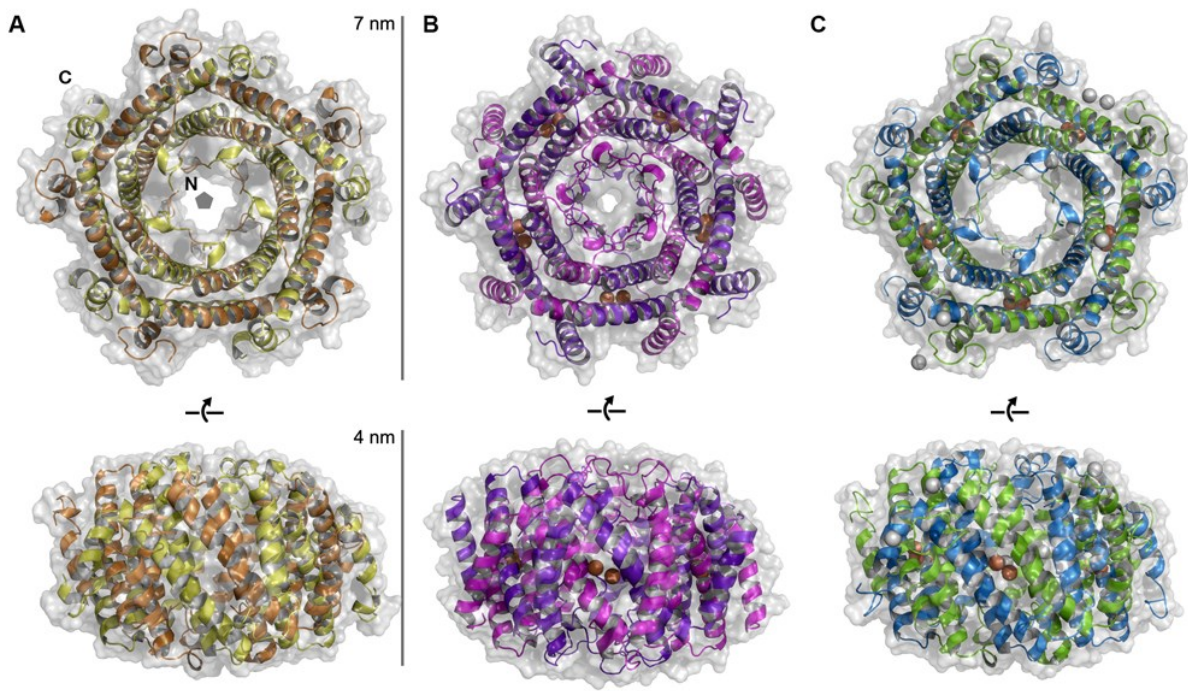
608 states (23+ to 31+) are highlighted with pink circles and monomer charge states (5+ to 17+) are

609 highlighted by blue circles. \* denotes the extended charge state observed. C: nESI spectrum of

610 Hoch\_EncFtn with gas phase oligomerization stressed with coloured circles. Monomer shown as

611 blue; dimer as green; tetramer as purple; hexamer as yellow and decamer as pink.

612



613

614 **Figure 3. Encapsulated ferritins from *Haliangium ochraceum* and *Pyrococcus furiosus* form**

615 **annular decamers.** The annular decameric architecture of the encapsulated ferritins from

616 *Haliangium ochraceum*, A, and *Pyrococcus furiosus*, B, are shown as transparent solvent

617 accessible surfaces over secondary structure cartoons. The published structure of the

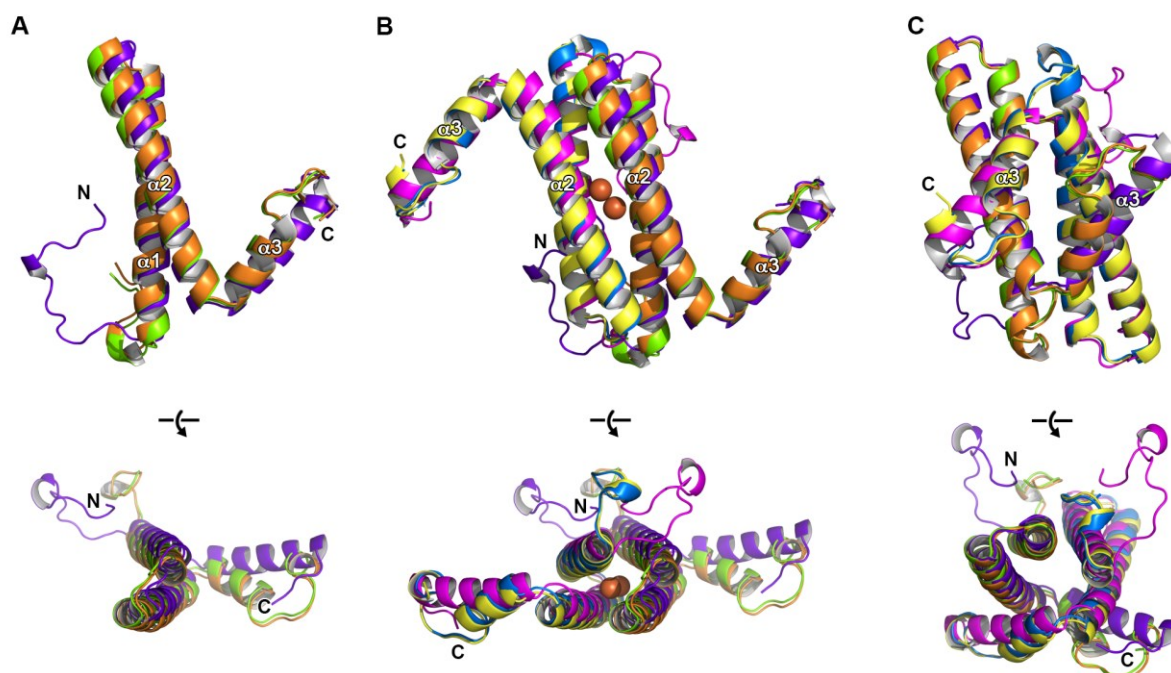
618 *Rhodospirillum rubrum* encapsulated ferritin is shown for comparison, C (PDB ID: 5DA5) [1].

619 Bound metal ions are shown as spheres: iron ions are depicted in orange, and calcium ions in

620 grey. The positions of the N- and C-termini of the protein chains and five-fold symmetry axis are

621 highlighted in panel A.

622



623

624 **Figure 4. Crystal structures of encapsulated ferritins from *Haliangium ochraceum* and**

625 ***Pyrococcus furiosus*.** Secondary structure cartoon depictions of the structures of the protomers

626 and dimers found in the crystal structures of the Hoch\_EncFtn and Pfc\_EncFtn encapsulated

627 ferritins. A, orthogonal views of the protomers: Hoch\_EncFtn shown in orange; Pfc\_EncFtn in

628 purple; and Rru\_EncFtn in green for comparison (PDB ID: 5DA5) [1]. B, orthogonal views of the

629 ferroxidase centre dimer. Iron ions present in the Pfc\_EncFtn dimer are shown as orange spheres.

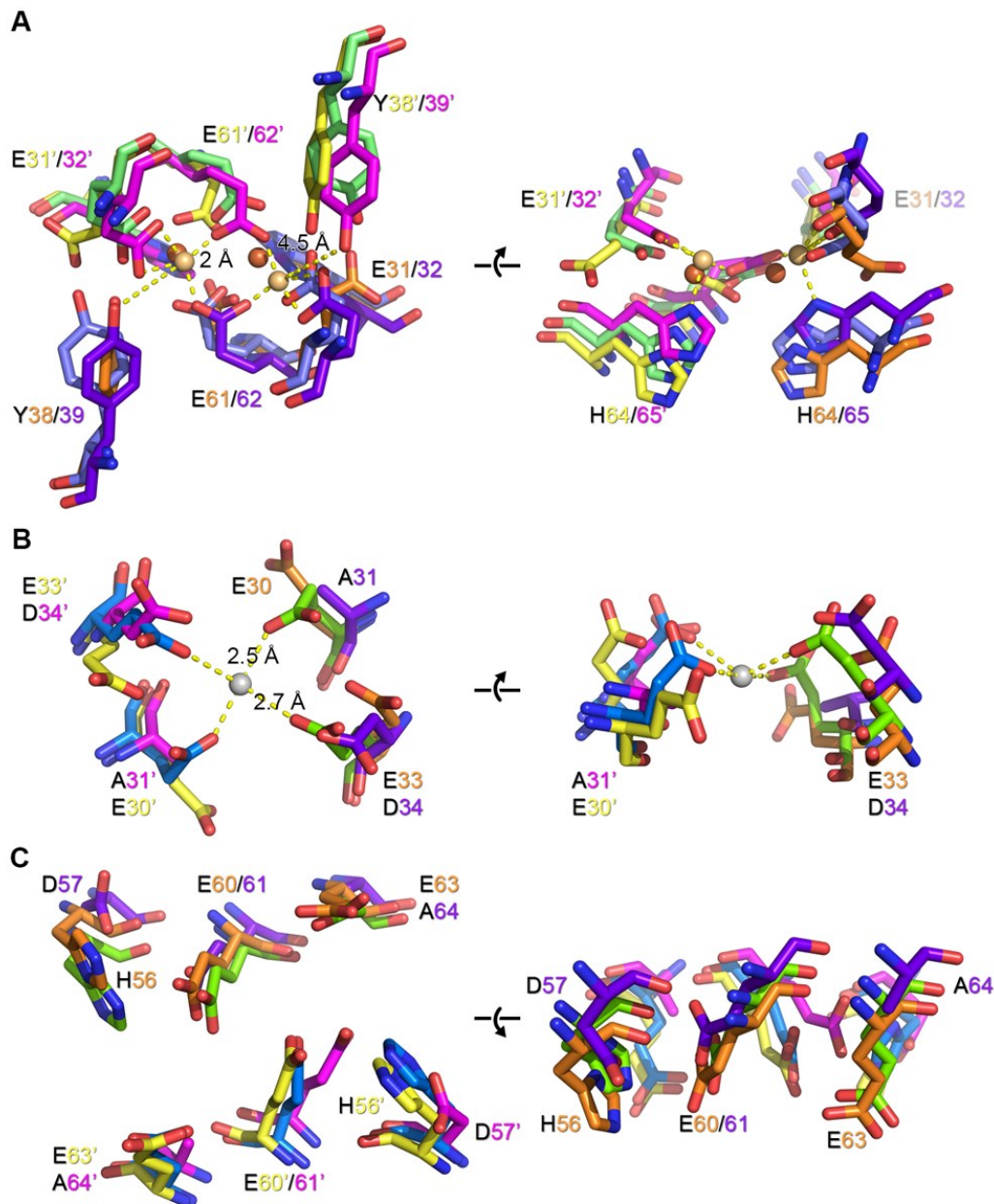
630 No metal ions were present in the Hoch\_EncFtn structure. Hoch\_EncFtn is shown in

631 orange/yellow; Pfc\_EncFtn in purple/pink; and Rru\_EncFtn in green/blue. C, orthogonal views of

632 the non-FOC dimer, depicted as in B.

633





634

635 **Figure 5. Ferroxidase centre and putative metal binding sites of encapsulated ferritins.**

636 Orthogonal views of the ferroxidase centre (A) and putative secondary metal binding sites (B/C) of

637 Hoch\_EncFtn (yellow/orange) and Pfc\_EncFtn (pink/purple) compared to Rru\_EncFtn (PDB ID:

638 5DA5) [1] (blue/green). A, conserved ferroxidase centre residues are numbered for Hoch\_EncFtn

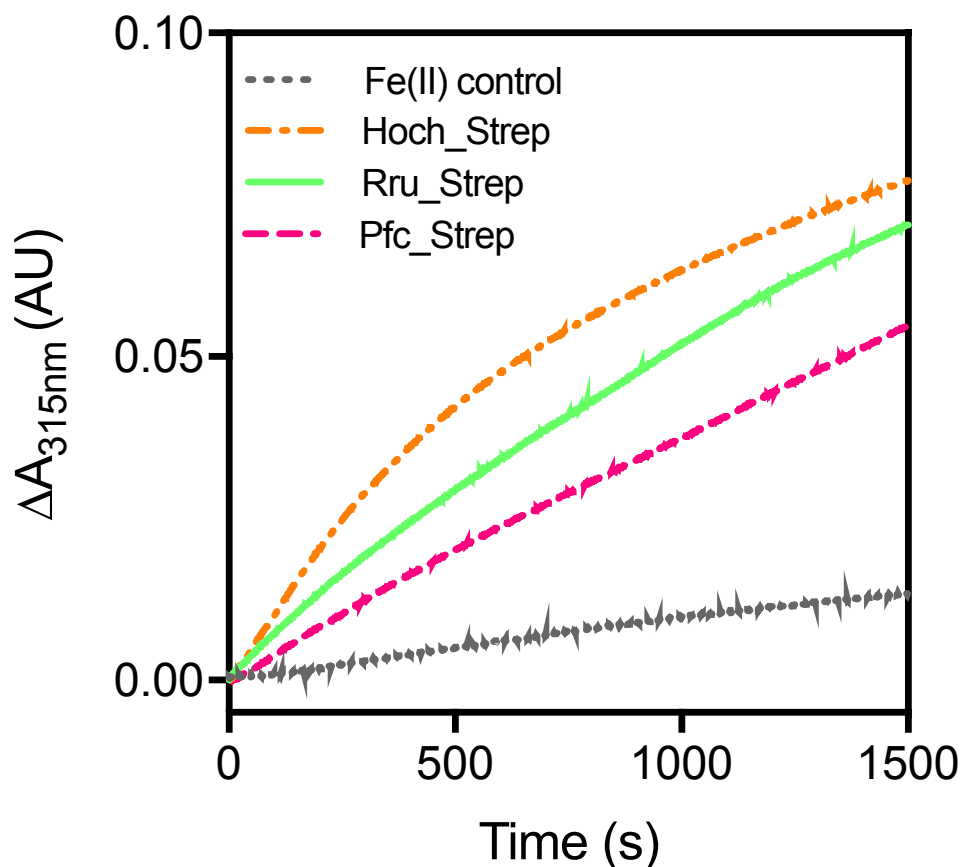
639 and Pfc\_EncFtn. Iron ions found in the Pfc\_EncFtn FOC are shown as gold spheres with

640 coordination distances to side chain atoms shown. The positions of the iron ions in the Rru\_EncFtn

641 structure are shown as orange spheres. B, residue conservation in the site occupied by calcium in

642 the Rru\_EncFtn structure (grey sphere, with coordination distances). C, conserved residues on the

643 outer surface of the encapsulated ferritin surface, located 10 Å from the FOC.



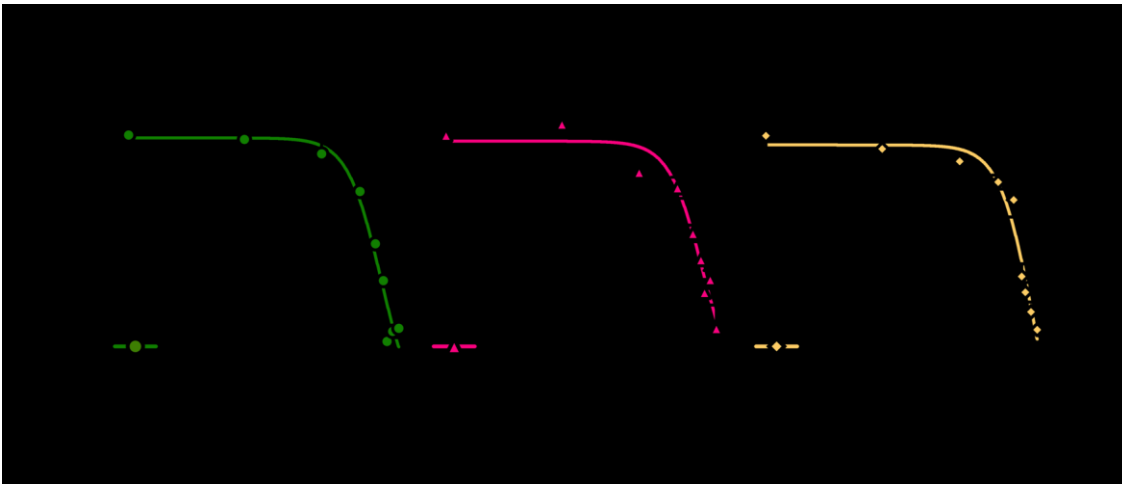
644

645 **Figure 6. Ferroxidase activity of encapsulated ferritins.** Hoch\_StrepII(dotdash orange line),  
 646 Pfc\_StrepII(dashed pink line), and Rru\_StrepII(solid green line) (10  $\mu\text{M}$  monomer) were incubated  
 647 with 50  $\mu\text{M}$   $\text{FeSO}_4 \cdot 7\text{H}_2\text{O}$  (10 times molar equivalent  $\text{Fe}^{2+}$  per FOC) and progress curves of the  
 648 oxidation of  $\text{Fe}^{2+}$  to  $\text{Fe}^{3+}$  was monitored at 315 nm. The background oxidation of iron at 50  $\mu\text{M}$  in  
 649 enzyme-free control is shown for reference (dotted grey line). Solid lines represent the average ( $n$   
 650 = 3) of technical replicates, shaded areas represent standard deviation from the mean.

651 DOI: 10.6084/m9.figshare.7718879

652





653

654 **Figure 7. The ferroxidase activity of encapsulated ferritins is inhibited by zinc. A, B, C, Non-**  
 655 linear fit of ferroxidase activities of Strep-tagged proteins inhibited by varying concentrations of  
 656 Zn(II) by GraphPad software using a Dose-Response (log(inhibitor) vs. response (three  
 657 parameters) equation. Response used in this analysis is the average of three technical replicates  
 658 per condition. Data shown were recorded after 1500 seconds from the start of the assay.  $IC_{50}$  and  
 659  $logIC_{50}$  have been calculated for each protein (Table S8). DOI:

660 [10.6084/m9.figshare.7718879](https://doi.org/10.6084/m9.figshare.7718879)

661

662

663